



HAL
open science

Solute effects on dynamics and deformation of emulsion droplets during freezing

Sidhanth Tyagi, Cécile Monteux, Sylvain Deville

► **To cite this version:**

Sidhanth Tyagi, Cécile Monteux, Sylvain Deville. Solute effects on dynamics and deformation of emulsion droplets during freezing. *Soft Matter*, 2022, 10.1039/D2SM00226D . hal-03274394v2

HAL Id: hal-03274394

<https://hal.science/hal-03274394v2>

Submitted on 31 May 2022 (v2), last revised 7 Jul 2022 (v3)

HAL is a multi-disciplinary open access archive for the deposit and dissemination of scientific research documents, whether they are published or not. The documents may come from teaching and research institutions in France or abroad, or from public or private research centers.

L'archive ouverte pluridisciplinaire **HAL**, est destinée au dépôt et à la diffusion de documents scientifiques de niveau recherche, publiés ou non, émanant des établissements d'enseignement et de recherche français ou étrangers, des laboratoires publics ou privés.

Solute effects on dynamics and deformation of emulsion droplets during freezing

Sidhanth Tyagi^{1,2}, Cécile Monteux², and Sylvain Deville³

¹*Laboratoire de Synthèse et Fonctionnalisation des Céramiques, UMR 3080*

CNRS/Saint-Gobain CREE, Saint-Gobain Research Provence, Cavaillon, France.

²*Sciences et Ingénierie de la Matière Molle, ESPCI Paris, PSL Research University,*

CNRS, Sorbonne Universités, UPMC Univ Paris 06, Paris, France.

³*Université de Lyon, Université Claude Bernard Lyon 1, CNRS, Institut Lumière*

Matière, 69622 Villeurbanne, France.

May 31, 2022

Abstract

Soft or rigid particles, suspended in a liquid melt, interact with an advancing solidification front in various industrial and natural processes, such as fabrication of particle-reinforced-composites, growth of crystals, cryopreservation, frost heave, and growth of sea ice. The particle dynamics relative to the front determine the microstructure as well as the functional properties of the solidified material. The previous studies have extensively investigated the interaction of foreign objects with a moving solid-liquid interface in pure melts while in most real-life systems, solutes or surface active impurities are almost always present. Here we study experimentally the interaction of spherical oil droplets with a moving planar ice-water interface, while systematically increasing the surfactant concentration in the bulk liquid, using *in situ* cryo-confocal microscopy.

We demonstrate that a small amount of surfactant in the bulk liquid can instigate long-range droplet repulsion, extending over a length scale of 40 to 100 μm , in contrast to the short-range predicted previously ($< 1 \mu m$). We report on the droplet deformation, while they are in contact with the ice-water interface, as a function of the bulk surfactant concentration, the droplet size, and the crystal growth rate. We also depict the dynamic evolution of solute-enriched premelted films ($\approx 5 \mu m$). Our results demonstrate how an increasing concentration of surfactant in the bulk and its subsequent segregation during solidification can dramatically alter the solidification microstructures. We anticipate that our experimental study can serve for the development of theoretical models incorporating solute effects.

Keywords: solidification, solute, droplets, deformation, dynamics

1 Introduction

The interaction of particles with an approaching solid-liquid interface is of special relevance in nature, like frost heave, glacial motion [1], and in engineering sciences, such as food freeze-thaw stability [2], cryopreservation [3, 4], metallurgy [5], and crystal growth [6]. This dynamic problem consists of particles, soft or hard, dispersed in a liquid melt interacting with a solid-liquid interface. The objects can be biological cells in cryopreservation [3, 4], colloids in freeze-casting [7], droplets in food preservation [8], gas bubbles in growth of single crystals [6, 9] and metallurgy [5], or reinforcing particles in material-matrix-composites [10]. The outcome of the particle-interface confrontation determines the solidified microstructure and hence, the functional properties of the solidified material.

It is essential to understand the underlying mechanisms of solidification (or freezing) to forge the required material microstructure. The particle can interact with an advancing solidification interface with diverse outcomes; it can be engulfed instantaneously upon contact, pushed ahead in the remaining liquid by

the interface indefinitely, or it may undergo engulfment after being pushed over a certain distance [11]. The shape of the particle (deformed or undeformed) becomes an equally important processing criterion in applications where soft deformable objects (droplets or bubbles) encounter a moving solid-liquid interface. Numerous interaction scenarios, still poorly understood, can therefore exist during solidification.

The role and concentration of solute in the solidifying liquid is often significant and a dominating factor in determining, amongst others, the shape of the solid-liquid interface in the vicinity of the suspended particles [12–14]. Solutes render the interfacial curvature concave, thereby promoting engulfment of objects at growth rates lower than those predicted for planar curvatures [15, 16]. The solutes can be either desired, like additives (e.g. cryoprotectant used in preservation of biological cells), or be present as an undesired impurity, such as dissolved gases (H_2) in liquid metals or surface active impurities. The segregation of solutes at the interface is instigated by their relatively low solubility in the solid phase and enhanced further by the approaching objects obstructing their diffusion field [12]. This local solute enrichment is of particular importance in understanding the nucleation and growth of macroporosity in solidifying melts [13], studying the constitutional supercooling with formation of premelted films [17, 18], and in determining the osmotic stresses acting on a freezing biological cell [4, 19] to give a few examples. Moreover, the morphology of a solid-liquid interface (planar, columnar, or dendritic), determined by the magnitude of solute concentration gradient build-up ahead of the growing solid, plays a major role on the final microstructure [12, 20].

The observation of particle pushing by a growing crystal instigated studies to deduce a critical velocity (V_c), the growth rate below which a particle is pushed ($V_{sl} < V_c$) and above which the particle is engulfed ($V_{sl} > V_c$) by the growing solid. Past studies have formulated a plethora of analytical and numerical models expressing the outcome (engulfment or rejection) of objects interacting at close distances ($< 10 \text{ nm}$) with the solid-liquid interface [15, 21–

24].

The prediction of a critical velocity in a given system depends on the nature and magnitude of various forces acting on the particle while it is being pushed by the solidification front. At steady-state repulsion, the sum of these forces must be zero, and the critical velocity will be reached when the forces are no longer in equilibrium. The models vary in the mathematical formulation of the features taken into account (e.g. the inclusion of object-melt thermal conductivity mismatch, solute effects etc. . .), while using a similar approach (balance of repulsive and attractive forces between the object and front) to describe the interaction [11]. In all these models, a short range repulsive interfacial (or thermomolecular) force is present. Particles start being repelled at very short distances (less than a micrometer) from the front.

The study of particle deformation has been of particular interest in the prediction of pore shape evolution during directional solidification of crystals to avoid or control porosity defects. Much of the progress in this domain has been achieved through numerical simulations and post-solidification analysis [25, 26]. *In situ* experimental evidence of solidification dynamics (repulsion or engulfment) and shape modification have been facilitated using transparent analogs (e.g. succinonitrile-acetone) with optical microscopes at ambient temperatures [20, 27] and X-ray transmission microscope at elevated temperatures [13, 28]. However, the volume investigated along with the temporal resolution is limited, while the local solute segregation cannot be visualized. Hence, the tracking of microstructures where objects interact with a solid-liquid interface in the presence of solute effects remains challenging.

In this study, we analyse the interaction of spherical oil droplets with an advancing ice-water interface using *in situ* cryo-confocal microscopy. We investigate the impact of an increasing surfactant concentration on the mechanisms involved at three different stages: droplets in water (water) far from the solidification front, droplets in contact with an approaching solid-liquid interface, and droplets captured in the growing ice. The three interaction stages are crucial

in determining the droplet spatial distribution and shape evolution, and hence, the solidification microstructure.

2 Methods

2.1 Materials

We purchased the oil (propyl benzoate), surfactant (Tween 80), oil fluorophore (Difluoro2-[1-(3,5-dimethyl-2H-pyrrol-2-ylidene-N)ethyl]-3,5-dimethyl-1H-pyrro lato-Nboron), and aqueous fluorophore (Sulforhodamine B) from Sigma-Aldrich. The fluorophores are referred to as BODIPY (incorporated in oil) and SRhB (incorporated in water) in the study. We cycled the deionized water through 0.45 μm Nylon membrane filters (VWR International) to remove traces of impurities and ensure purity of the emulsions prepared. We chose propyl benzoate owing to its low melting temperature ($T_m = -51.6^\circ \text{C}$), low solubility in water (0.035 g/100 g), and similar density to water ($\rho_{oil} = 1.023 \text{ g} \cdot \text{cm}^{-3}$).

2.2 Sample Preparation

We prepared the oil-in-water emulsions using a microfluidic setup, as explained in our previous study [14]. The monodisperse droplets have radii (R_1, R_2) of either $7.2 \pm 0.4 \mu\text{m}$ or $30.9 \pm 1.2 \mu\text{m}$, as shown in Supporting information. The oil phase consisted of propyl benzoate with 10^{-4} M BODIPY to obtain clear imaging of dispersed droplets at 1% laser power. For the aqueous phase, we used 10^{-5} M SRhB solution, as self-quenching was reported at concentrations above $2 \times 10^{-4} \text{ M}$ [29]. We added Tween 80 ($HLB = 15$ [30]), a non-ionic surfactant, to the aqueous phase to stabilise the oil droplets. The surfactant Tween 80 ($cmc = 13 - 15 \text{ mg} \cdot \text{l}^{-1}$ [31]) also acts as a solute and hence colligatively depresses the freezing point of solutions, when its concentration increases locally [14]. We prepared three aqueous solutions with 0.01, 0.1, and 1 wt.% Tween 80 to study the impact of solute concentration on the solidification dynamics and behaviour of oil droplets dispersed in an aqueous phase. The surfactant is added as wt.% of

the aqueous solution to have an equal concentration in all the solutions prepared.

The concentration of surfactants in the bulk solution at which micelles start forming is known as the *cmc*. Individual surfactant molecules that are in the system but are not part of a micelle are called monomers [32]. At 1wt.% of Tween 80 in aqueous solution we are $\approx 600\times$ *cmc*. All experiments are therefore performed above the *cmc* and increasing the surfactant concentration results in an increase of the number of micelles in solution while the concentration of surfactant monomers remains approximately equal to the *cmc*. The presence of micelles at the given concentration was confirmed by dynamic light scattering (DLS) analysis. A typical micelle size of 9 nm with a corresponding diffusion coefficient of $30 \mu\text{m}^2 \cdot \text{s}^{-1}$ at 273 K was obtained from the DLS analysis. The prepared emulsions were filled through capillarity and solidified in a rectangular Hele-Shaw cell (height =100 μm and volume =100 μl). We fabricated the Hele-Shaw cell using two glass slides (Menzel, 24×60 mm, thickness 0.13–0.16 mm), and sealed it with nail-polish at one end to prevent evaporation and leakage.

2.3 Imaging & Analysis

We used a Leica TCS SP8 confocal laser scanning microscope (Leica Microsystemes SAS, Germany) equipped with 488 nm (blue), 552 nm (green) lasers and two photodetectors (PMT) for image acquisition. The images were captured for the emission spectra of BODIPY (oil phase) and SRhB (aqueous phase), using a non-immersive objective (Leica HCX PL APO CS 20 \times) with a working distance of 590 μm . Ice does not fluoresce and hence the confocal image enables us to distinguish three phases; oil droplets in cyan, water in colormap veridis and a dark ice phase. In 2D, we used the microscope at a scanning speed of 600 Hz, with 1024×1024 pixels for imaging $775 \times 775 \mu\text{m}$, resulting in 1.7 s per frame. We used Fiji [33] for image thresholding in conjunction with Python [34] for image and data analysis.

2.4 Freezing Stage

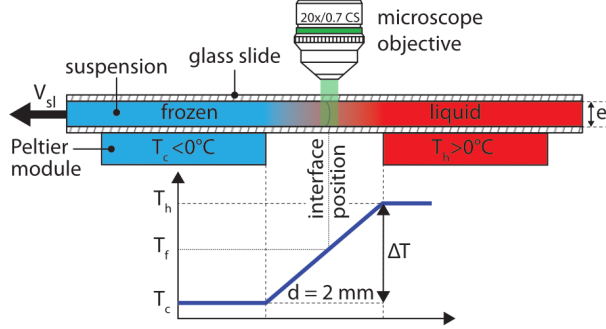


Figure 1: **Cryo-confocal microscope setup to perform *in situ* solidification experiments.** A Hele-Shaw cell containing an oil-in-water emulsion is pulled at a constant velocity (V_{sl}) through a constant linear temperature gradient (G), established by two Peltier elements. In *steady-state*, the solidification interface is at a constant position under the microscope objective.

We conducted unidirectional solidification experiments, translating the sample cell at a constant velocity (V_{sl}) along a constant linear temperature gradient (G) of $10^4\text{ K}\cdot\text{m}^{-1}$, using the cryo-confocal stage described in detail previously [35]. We imposed the temperature with two Peltier modules, and controlled it with high precision ($< 0.01\text{ }^\circ\text{C}$) using TEC-1122 Dual Thermo Electric Cooling Temperature Controller from Meerstetter Engineering, Switzerland. The Peltier elements were separated by a distance of 2 mm to establish a linear temperature gradient. The *in situ* observation of objects interacting with the solid-liquid interface was achieved using a confocal microscope mounted vertically over the gap (2 mm) between the two Peltier modules, as shown in Fig. 1. Using this set up the solidification interface appears immobile in the frame of observation. We utilised the VT-80 translation stage (Micos Pollux Drive PI, USA) to impose the rate at the which the sample cell is pulled through the temperature gradient. The rate of translation was verified to be in agreement with the measured solidification velocity (V_{sl}), using posterior image analysis (*error* $< 1\%$). Thus, we can decouple and control independently the solidification velocity (V_{sl}) and the thermal gradient (G) in our system.

We performed the solidification experiments in the velocity range of $1.0 \mu\text{m} \cdot \text{s}^{-1} \leq V_{sl} \leq 10.0 \mu\text{m} \cdot \text{s}^{-1}$. We wait for 20–30 mins to ensure a *steady-state* diffusion controlled regime before starting the acquisition at a given solidification velocity. The time needed for a steady-state to establish scales as $2D/V_{sl}^2 \approx 60 \text{ s}$, where D is the solute diffusion coefficient. We do not expect forced convection in our experiments as they are performed in a closed Hele-Shaw cell of small thickness ($100 \mu\text{m}$) and at low solidification velocity with a steady linear temperature gradient. The solid-liquid interface is stable over extended time periods ($\approx 4\text{--}5$ hours) and the interface does not accelerate or decelerate during the solidification experiments. In addition, we do not observe a transient unsteady regime and the interface morphology is stable for the given experimental parameters.

3 Results & Discussions

We performed horizontal solidification experiments by displacing a Hele-Shaw cell, containing an oil-in-water emulsion, with our custom cryo-confocal stage, at a velocity of V_{sl} . A typical $2D$ confocal image of a freezing emulsion with the distinct features observed is shown in Fig. 2A. As solidification progresses, the growing ice phase rejects the dissolved dye, SRhB, owing to its low solubility and hence appears black, which enables us to visualize the solid-liquid interface. In the frame of observation, the interface is stationary. In the frame of the sample, the interface is advancing through the sample at a velocity of V_{sl} along \vec{x} and eventually encounters droplets which velocity, noted U_r (defined in Fig. S2) is indicated in Fig. 2A. We also note the premelted films between two ice surfaces as well as around the oil droplets captured in the ice phase, which are due to the rejection of the dye by the ice and subsequent depression of the freezing point.

A typical time-lapse evolution of an isolated oil droplet interacting with the ice-water interface obtained for an oil-in-water emulsion with $1\text{wt.}\%$ Tween 80 in the aqueous phase is shown in Fig. 2B. The interaction of oil droplets

with the solid-liquid interface can be divided in three different stages, which are described below in three different sections and which dynamics depends on the surfactant concentration and advancing velocity. First, we investigate the solidification mechanisms at play when the oil droplets in the water phase far from the advancing interface. Secondly we report the evolution of the droplet shape upon contact with the interface. Third we analyse the droplets captured in ice and report on the evolution of premelted films with the associated ice-water meniscus.

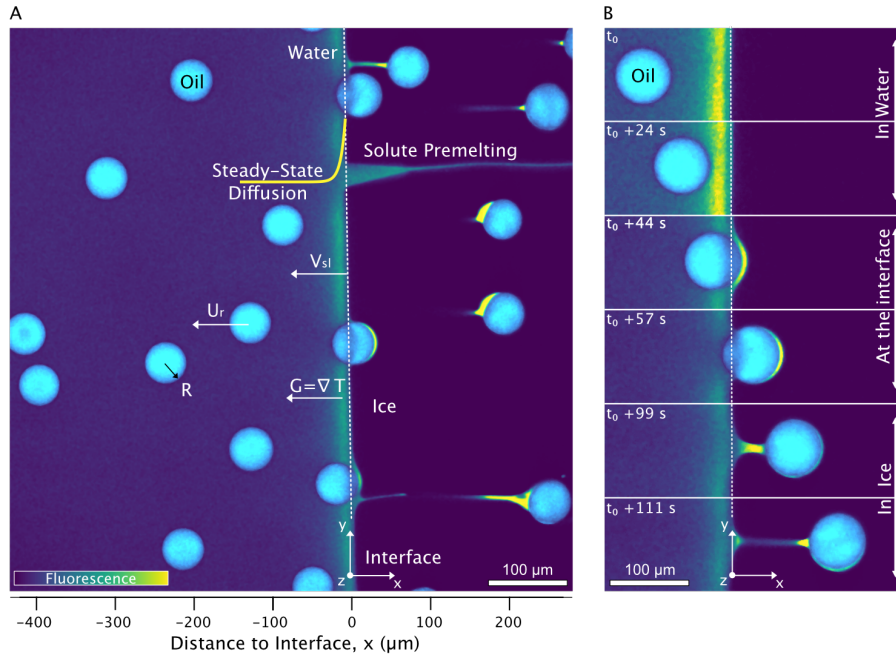


Figure 2: **2D cryo-confocal image of freezing an oil-in-water emulsion in the presence of 1wt.% Tween 80 in the aqueous phase.** (A) Typical features observed for a planar growth at $V_{sl} = 2 \mu\text{m} \cdot \text{s}^{-1}$ (B) Time-lapse evolution of an oil droplet encountering an approaching solid-liquid interface with three distinct regimes of interaction at $V_{sl} = 2 \mu\text{m} \cdot \text{s}^{-1}$. Ice is in black, oil droplets in cyan, and the aqueous phase is in colormap viridis (fluorescence bar). © (2020) S. Tyagi *et al.* (10.6084/m9.figshare.14815083) CC BY 4.0 license <https://creativecommons.org/licenses/by/4.0/>.

3.1 Droplets in water

From each experiment, we acquire 50–400 droplet trajectories and for each trajectory we measure the droplet velocity in the frame of observation $U' = \delta x / \delta t$ with x being the distance to the interface and t the time (see Fig. S1 for the definition of x and t). We then deduce the velocity of the droplets in the sample frame $U_r = V_{sl} - U'$. We then average over 50 – 400 droplets to obtain the mean velocity $\bar{U} = \langle U_r \rangle$ (see details in Fig. S2 and Reference [18] for the python script). Using these notations, a positive magnitude of \bar{U} implies that the droplets are repelled or pushed by the moving ice-water interface towards the remaining liquid.

In Fig. 3, we present the mean droplet velocity, \bar{U} , with the distance to interface for an interface velocity of V_{sl} of $3 \mu\text{m} \cdot \text{s}^{-1}$. We define the distance to interface as $0 \mu\text{m}$ when the front edge of the droplet comes in contact with the absolute detected position of the ice-water interface.

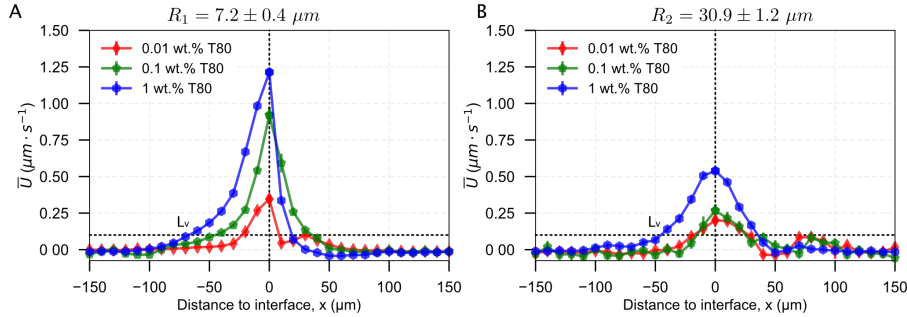


Figure 3: **Droplet dynamics in presence of 0.01, 0.1, and 1wt.% solute in solution, deduced from the droplet trajectories at $V_{sl} = 3 \mu\text{m} \cdot \text{s}^{-1}$.** Mean droplet velocity versus distance to interface for (A) $R_1 = 7.2 \pm 0.4 \mu\text{m}$ and (B) $R_2 = 30.9 \pm 1.2 \mu\text{m}$. The droplets accelerate as the solidification front approaches, and decelerate as they are engulfed into the ice. © (2020) S. Tyagi *et al.* (10.6084/m9.figshare.14815083)

At large distances from the interface, larger than $100 \mu\text{m}$ the droplets in water are unperturbed and their mean velocity \bar{U} in the sample frame is zero. As they get closer to the interface, they start getting repelled. The mean droplet velocity (\bar{U}) increases and exhibits a maximum (U_{max}), when the leading edge

of the droplets coincides with the initial position of the growing crystal. We note that the droplet velocity \bar{U} is lower than V_{sl} , which means that the droplets are finally captured in ice. As the droplets are captured in ice, their velocity \bar{U} returns to zero. As shown in Fig. 3, \bar{U} decreases for a larger droplet size, while it increases with an increasing surfactant concentration.

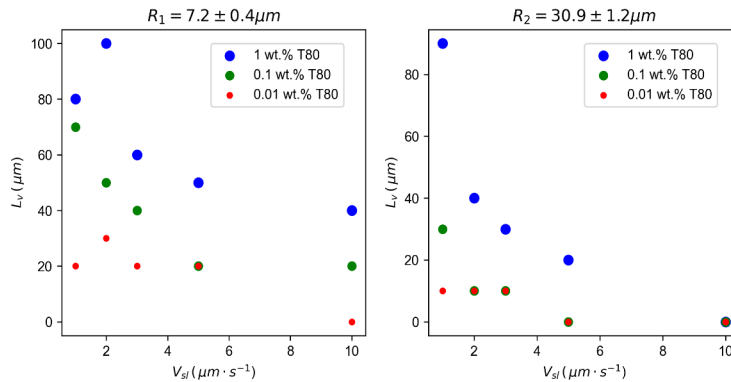


Figure 4: **Characteristic length scale L_v versus Solidification Velocity (V_{sl}), for different solute concentrations (wt.%).** Left: $R_1 = 7.2 \pm 0.4 \mu m$ and right: $R_2 = 30.9 \pm 1.2 \mu m$ droplets. The distance L_v , where droplets in water start getting repelled by the interface, increases significantly with the solute concentration, while it decreases with an increasing growth rate. © (2020) S. Tyagi *et al.* (10.6084/m9.figshare.14815083).

From the evolution of \bar{U} with the distance to the interface, we define a characteristic length scale, L_v , corresponding to the distance at which the droplets attain a mean velocity (\bar{U}) of $0.1 \mu m \cdot s^{-1}$, which is shown in Fig. 4. This distance corresponds to the range of interaction between the droplets and the interface. We find that the droplets get repelled over distances ranging between 10 and $100 \mu m$, often larger than their diameter, especially for the largest surfactant concentrations. Smaller droplets with radius R_1 are repelled at greater distances from the interface as compared to the larger R_2 droplets. Increasing the growth rate decreases the characteristic distance L_v .

The results described so far show that an increasing amount of surfactant induces a repulsion of the droplets by the interface over large distances, of the order of ten to a hundred of microns away from the interface and that the droplet

dynamics is influenced by the bulk surfactant concentration, the growth rate and the droplet size. These three parameters control the surfactant concentration profile close to the solidification front. Indeed the surfactant is poorly soluble in the ice therefore it is rejected and accumulates close to the front. In a steady state regime where a solidification front advances at a velocity V_{sl} the distance L_d over which the rejected solute accumulates scales as $L_d=D/V_{sl}$ with D the diffusion coefficient of the solute [36] and results from a competition between the advection velocity which favors the accumulation of solute close to the front and the diffusion of the solute which tends to reduce the gradient.

Assuming no convection in the liquid and no diffusion of the solute in the solid, the concentration field of rejected solutes in the remaining liquid writes

$$C_L = C_0 + C_0 \left(\frac{1 - K_0}{K_0} \right) \exp \left[\frac{-V_{sl}}{D} |x| \right] \quad (1)$$

where C_L is the solute concentration at a distance x from the interface and C_0 is the bulk solute concentration in the liquid far from the interface [36]. K_0 , the partition coefficient, is related to the solubility of the solute in the ice and is defined as the ratio of surfactant concentration in the solid phase to the one in the liquid. A low solubility in ice and a large partition coefficient favor the accumulation of surfactant in the melt phase close to the front.

In a previous article [18], we discussed that the displacement of the droplets may be caused by surfactant concentration gradients close to the ice-water interface, either through a phenomenon called diffusiophoresis [37] or through Marangoni flow at the droplets/water interface. However the surfactant concentration used in this study is largely above the CMC (critical micellar concentration) therefore we do not expect large variations in surfactant monomer concentration and hence of the surface tension as a function of the surfactant concentration. We rather suggest that a large variation in the micelle concentration close to the front could induce a diffusiophoretic motion of the drops as suggested in our previous article.

Diffusiophoresis is provoked by solute concentration gradients and can lead to displacement of micrometric particles with velocities of the order of a few micrometers per second, comparable to the droplet velocities that we measure in our study. From Eq. (1), it is expected that the local gradient of surfactant concentration spans over a typical distance $L_d = D/V_{sl}$ [36]. Hence an increasing growth rate (V_{sl}) will decrease the distance at which the solute field can be perceived by the droplets and can qualitatively account for the decreasing values of L_v measured (see Fig. 4) at high growth rates. Moreover the concentration gradient $C_L - C_0$ depends linearly on C_0 which can possibly account for the strong influence of the surfactant concentration on the droplet displacement.

We first examine the validity of Eq. 1 by recording the fluorescence intensity of the fluorescent dye, SRhB, which can be obtained easily with the confocal microscope and which diffusion coefficient is equal to the one of the surfactant monomers (see Fig. 5A).

The concentration profile of SRhB rejected by the ice-water interface, deduced from the fluorescence intensity profile for a growth rate of $3 \mu m \cdot s^{-1}$ is given in Fig. 5B. At $3 \mu m \cdot s^{-1}$, the concentration profile obtained is in agreement with the *steady-state* diffusion profile predicted from Eq.1 (see Fig. 5B) with a distance L_{dye} of the order of $150 \mu m$.

However we note that the experimental and theoretical profiles do not match at higher velocities (not shown) probably because of constitutional undercooling which modifies the freezing temperature of the melt, hence the local temperature close to the front and the diffusion coefficient of the dye.

Interestingly, we see from Fig. 4 that the distance L_v over which both the large and small droplets get repelled from the interface is below $60 \mu m$ for a front velocity of $3 \mu m \cdot s^{-1}$, hence it is much smaller than the accumulation distance expected for the surfactant monomer and the dye, as shown in Fig. 5B and which is of the order of $L_{dmonomer} = 150 \mu m$.

Taking the diffusion coefficient of micelles measured with DLS, instead of the one of the surfactant monomers, we find a lower value of the accumulation

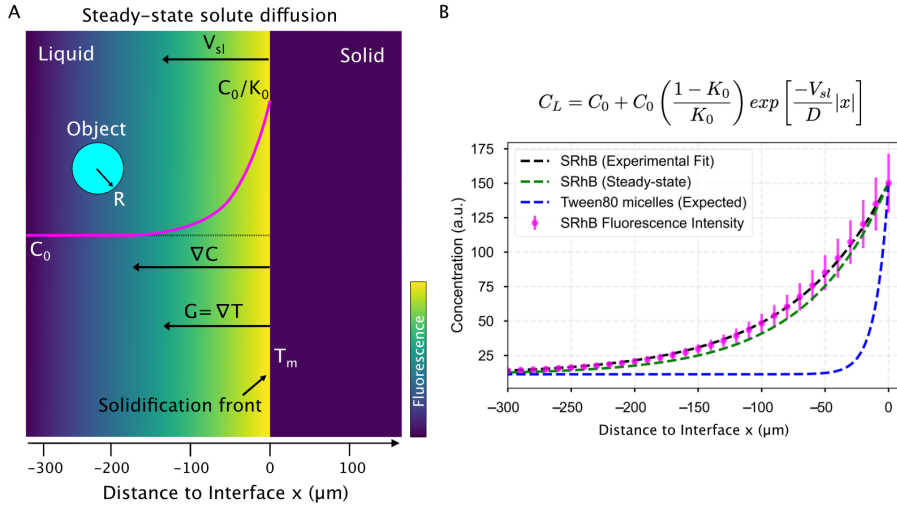


Figure 5: **Solute rejected by the growing solid phase and segregated at the solid-liquid interface during *steady-state* directional solidification.** (A) Model sketch depicting the concentration profile evolution of a solute (in magenta) in the remaining liquid, rejected by a solidification front advancing at V_{sl} , during *steady-state* planar growth. (B) Mean fluorescence intensity (magenta) of SRhB, acquired using a confocal microscope, is fit with a theoretical diffusion-type exponential (black line). The predicted *steady-state* diffusion of SRhB (green line), using the model from Tiller *et al.* [36], corresponds closely to the experimental data fit. A *steady-state* planar growth is thus verified. The corresponding *steady-state* diffusion profile of Tween 80 micelles (blue) shows a significant difference in length scales over which the two molecules (SRhB and Tween 80) diffuse. All data presented was recorded for a growth rate of $3 \mu\text{m} \cdot \text{s}^{-1}$. © (2020) S. Tyagi *et al.* (10.6084/m9.figshare.14815083).

length L_d . As shown in Fig. 5B, at a growth rate of $3 \mu\text{m} \cdot \text{s}^{-1}$, we obtain a typical distance $L_{d \text{ micelle}}$ of $10 \mu\text{m}$, which is lower than the distance L_v measured experimentally at this growth rate from Fig. 5B. Hence it turns out that the experimental value of L_v ranges between $L_{d \text{ micelle}}$ and $L_{d \text{ monomers}}$ calculated for the surfactant micelles and monomers respectively. We note that the situation is in fact very complex. Indeed as Equation 1 predicts different concentration profiles for the surfactant monomers and micelles we expect that fresh micelles may form over distances of the order of $L_{d \text{ monomers}}$ where the monomers accumulate while these micelles are advected closer to the front to reach $L_{d \text{ micelles}}$. We expect that the exchange dynamics between the surfactants and the micelles will therefore play a key role in the actual micelle concentration profile.

We note that diffusiophoretic displacements of particles and drops have been studied theoretically and experimentally for ionic solutes such as ionic salts, charged surfactants such as Sodium dodecylSulfate or CO_2 that dissolves into ionic species [37–40]. The case of non-ionic species has also been studied but not non-ionic surfactants hence it is difficult to predict the expected behaviour in our case [41, 42]. Nevertheless we note that the diffusiophoretic velocity is usually expected to increase with the size of the particle [43–45] while in our case we observe that smaller droplets move with a higher velocity (Fig. 4). It should be noted that when the droplets come in close contact with the front the concentration profile in the gap between the drop and the front may be modified. Indeed the presence of the droplets may obstruct the diffusion of surfactant away from the front hence favoring the accumulation of surfactants. On the other hand the advection of drops toward the front may also induce a radial squeeze flow pushing the solute out of the gap and redistributing the solute on the side of the drops. We therefore expect that the redistribution of solute between the drops and the front depends on the droplet size in a non trivial way.

To conclude this section the segregation of solute at the interface plays a key role in redistributing the droplets before they hit the solidification front. The object dynamics and impact of solute (or impurity) are still complex to quantify as the observation of solidification *in situ* remains challenging. We have tried to advance towards an *in situ* quantification of the solute mechanisms at play and further work is required to correlate the dye fluorescence intensity to the absolute solute concentration gradient. The latter can be useful in predicting thermal convection and non *steady-state* solidification regimes.

3.2 Droplets at the interface

We now focus on the behaviour of droplets when they come in contact (distance to interface = 0 μm) with the solid-liquid interface. We observe three typical behaviours of oil droplets as they encounter an approaching front, as shown

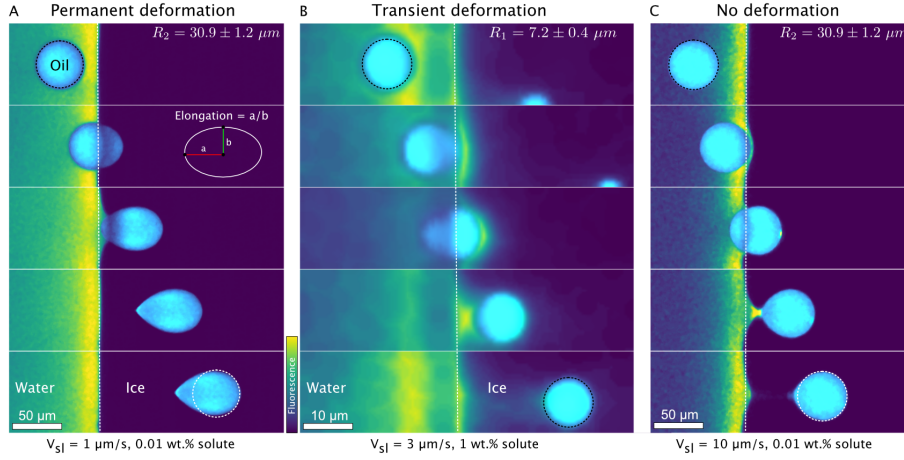


Figure 6: **Typical time-lapse montage depicting the three types of deformation behaviour of oil droplets while undergoing directional planar front solidification.** (A) The droplets elongate at the ice-water interface and remain deformed in the ice phase, scale bar = $50 \mu m$, time interval between frames: $44.5s$ (B) The droplets deform in a transient manner ($t = 13 s$) at the ice-water interface and recover their shape as they are captured by the growing ice phase, scale bar = $10 \mu m$, time interval between frames: $6.7s$ (C) The droplets do not undergo deformation and preserve their shape during their interaction and further engulfment in the growing crystal. Scale bar = $50 \mu m$, time interval between frames: $3.3s$. Oil is in cyan, water is in colormap viridis (fluorescence bar), and ice is in black. © (2020) S. Tyagi *et al.* (10.6084/m9.figshare.14815083).

in Fig. 6. The droplets can elongate permanently as they get engulfed in the growing ice (Fig. 6A), the droplets may deform transiently ($t = 13 s$) at the ice-water interface and subsequently relax to their original spherical shape as they move further into the ice phase (Fig. 6B), or the droplets remain mostly spherical during their engulfment by the growing crystal (Fig. 6C). We notice that the deformation behaviour depends on the droplet size R , the imposed growth rate V_{sl} , and the bulk surfactant concentration. Therefore, we need to systematically study the effect of these solidification parameters to understand the different types of deformation observed.

The droplet deformation is estimated from the analysis of $2D$ shape elongation, as shown in the schematic in Fig. 6A, taking the ratio of droplet diameters along \vec{x} and \vec{y} . In Fig. 7, we depict the mean elongation profiles calculated for 50

to 400 (depending on R and V_{sl}) droplet interactions in 0.01 *wt.*% and 1 *wt.*% solute solution at varying growth rates for two different droplet sizes (R_1, R_2).

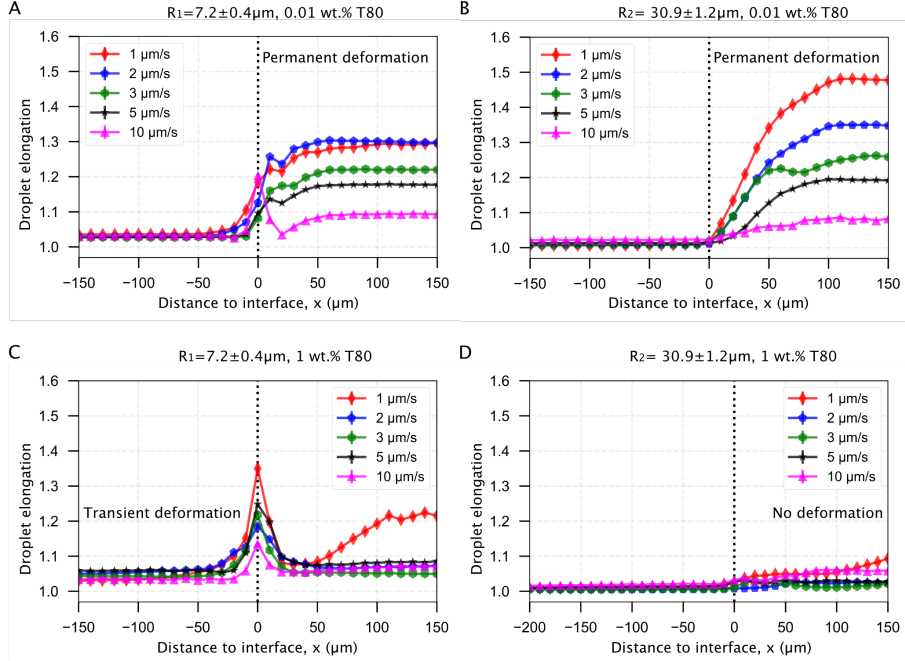


Figure 7: **Mean elongation profiles for oil droplets encountering an approaching ice-water interface.** Planar solidification front induced permanent deformation of oil droplets dispersed in a solution with (A,B) 0.01 *wt.*% solute concentration having a size of (A) $R_1 = 7.2 \pm 0.4 \mu\text{m}$ (B) $R_2 = 30.9 \pm 1.2 \mu\text{m}$. The transient and no deformation regimes for droplets in (C,D) 1 *wt.*% solute concentration having a size of (C) $R_1 = 7.2 \pm 0.4 \mu\text{m}$ (D) $R_2 = 30.9 \pm 1.2 \mu\text{m}$. © (2020) S. Tyagi *et al.* (10.6084/m9.figshare.14815083).

We observe from Fig. 7A and Fig. 7B that the droplets undergo permanent elongation for the two droplet sizes (R_1, R_2), when the bulk surfactant concentration is 0.01 *wt.*%. The elongation is ≈ 1.0 , representing a circle, when the droplets are in the remaining liquid far from the interface. The droplets start getting elongated as their front edge touches the interface (distance = 0 μm) and their shape transforms into an ellipse (elongation > 1.0). The droplet deformation evolves further and reaches a constant magnitude when the front edge is located at a distance of $2R \times \text{Elongation}$. Once the droplets are completely engulfed in the ice, their shape does not evolve any more (Fig. 7A,B). Interestingly, we notice that the elongation reduces with an increasing growth rate for

both the droplet sizes investigated. However, the maximum elongation for the smaller R_1 droplets is lower as compared to the larger R_2 droplets at the given 0.01 *wt.%* solute concentration.

In Fig. 7C, we report the transient deformation of the oil droplets as they confront the ice-water interface with 1 *wt.%* bulk solute concentration. Here, the oil droplets undergo elongation at the interface (distance = 0 μm) but eventually recover their shape as they are completely engulfed in the ice. In contrast, from Fig. 7D we notice that the larger R_2 droplets do not undergo any type of deformation at the same solute concentration of 1 *wt.%*. Hence, the elongation profile of R_2 droplets remains unmodified during the droplet-interface confrontation.

We deduce from these observations that the droplets confronting an approaching interface have distinct behaviours depending on the concentration of solute in the bulk solution. In particular, an increasing solute concentration tends to decrease the droplet elongation significantly.

Several experimental and theoretical studies devoted to the shape of bubbles during solidification in the absence of surfactant can be found in the literature [46–48]. Highly elongated bubbles along with the formation of a highly curved tip at the bubble-ice interface were observed [46, 47] and are controlled by the contact angle between the bubbles and the ice-water interface [48]. In the case of the low surfactant concentrations, we see from Fig. 6A that the contact angle between the droplets and the ice-water interface remains close to 90° during engulfment, similarly to bubbles, because of the weak thermal flux in the droplets owed to their low thermal conductivity in comparison to water [49]. This results in tear-shaped drops which are very similar to those reported in the literature for bubbles.

At higher surfactant concentration we observe much lower elongations. According to Eq.1, an increasing bulk solute concentration (C_0) implies a higher concentration of the solute segregated (C_0/K_0) at the solid-liquid interface. The segregation of solute is further enhanced owing to an obstruction of their diffu-

sion field by the droplets in the vicinity of the solid-liquid interface [12,50]. The segregated solute, trapped in the layer between the droplet and the interface, induces solute premelting [51,52] (Fig. 2B at $t = 44$ s, Fig. 6B at $t = 8$ s, in Fig. 6C at $t = 3$ s) which in turn causes a lowering of the equilibrium melting temperature of water. Therefore these premelted films are stable below the solid's bulk melting temperature, T_m and the thickness of the premelted films increases with the solute concentration [17,51]. As a premelting film intercalates between the droplets and the solid liquid interface, the situation is very different from the literature studies discussed above as no finite contact angle between the drops and the interface can be defined. Here we suggest that the liquid-liquid interfacial tension between the droplet and the premelting film favors spherical shapes to minimize the interfacial area. Interestingly we note that the effect of size is different at low and high surfactant concentrations. At low surfactant concentrations, smaller droplets undergo a lower deformation, probably because of a higher capillary pressure inside the drops that opposes the deformation. At opposite, for large surfactant concentrations, smaller droplets present a transient deformation, while larger droplets remain mostly spherical. This effect may be linked to the stronger segregation of solute in the films between the droplets and the ice in the case of larger films.

The deformation of droplets at the ice-water interface depends strongly on the growth rate (V_{sl}) and the corresponding bulk solute concentration (C_0). Furthermore, the addition of solute increases the thickness of the observable premelted films, which appears to act as a protection mechanism against the interface initiated droplet deformation. The local solute environment and deformation are two important criterion for cryopreservation in particular. In cryobiology, the excess of solute causes severe osmotic stresses that can instigate cell membrane rupture and hence, cryoinjury to cells and tissues [4,19]. In food engineering, alterations to the continuous phase concentration or to the shape and size of dispersed droplets is detrimental to the freeze-thaw stability of consumable emulsions [8]. Hence, a complete understanding of the solute

redistribution mechanisms along with the associated object deformation at the corresponding freezing conditions is desired. Our multi-dimensional approach highlights the importance of different solidification parameters and the ubiquitous role of solute in dominating the various aspects of object deformation behaviour. Further work is required to accurately estimate the direction and magnitude of forces at the origin of the observed deformation.

3.3 Droplets in Ice

We have discussed so far the dynamics and consequences of oil droplets interacting with an approaching ice-water interface. In the last section, we investigate the fate of droplets after their engulfment by the ice front.

At 1 *wt.*% solute in the aqueous solution, at a growth rate of $1 \mu\text{m} \cdot \text{s}^{-1}$, the droplets undergo an elongation process after engulfment whereby the two radii, along \vec{x} and \vec{y} , are stretched in magnitude as the droplets progress further in ice. This means that the droplets flatten in the z direction as they are engulfed in the ice. We depict this phenomenon with a time-lapse montage, highlighting the deformation, in Fig. 8. Interestingly, we observe this phenomenon only at a growth rate of $1 \mu\text{m} \cdot \text{s}^{-1}$ in the presence of 1 *wt.*% bulk solute concentration for both droplets radii R1 and R2.

We currently have no definitive explanations for this behavior. One possibility could be that the shape of the water/ice meniscus in these conditions (curved meniscus) may favor entrapment and flattening of the droplets between the ice and the glass surface. However, this particular point would deserve additional experiments, in particular in 3D, which are beyond the scope of the current study.

Furthermore we note that once the droplets are trapped in the ice, we do not observe any thermal regelation, i.e the droplets do not manifest any motion relative to the ice. Moreover the liquid layer between the droplet from the growing solid decreases in thickness as the droplets move along the temperature gradient in ice towards an increasing undercooling ($\Delta T = T_m - T$, where T is

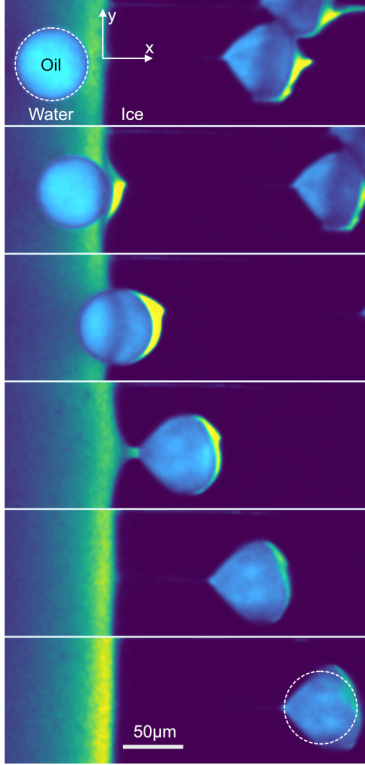


Figure 8: **Crushing of oil droplets during their engulfment in ice at a growth rate of $V_{st} = 1 \mu\text{m} \cdot \text{s}^{-1}$ with 1 wt% solute in solution.** $R_2 = 30.9 \pm 1.2 \mu\text{m}$. Typical time-lapse montage depicting the crushing of an oil droplet, scale bar = $50 \mu\text{m}$, time interval between frames: 60s. The dashed circle indicate the shape of the droplet before encapsulation. Note that in the crushing regime, the droplets are elongated in a direction parallel to the front, unlike in the other regimes (elongation perpendicular to the front). © (2020) S. Tyagi *et al.* (10.6084/m9.figshare.14815083).

the temperature of the substrate) [1]. The study of particle migration in ice is an important topic of research to understand frost heave, glacier motion, and ice-core dating among other technological applications [1]. Recent studies suggest that the presence of impurities or solutes tend to accelerate the *regelation* of trapped particles in ice. Typical migration velocities of $0.1 \mu\text{m} \cdot \text{s}^{-1}$ at ΔT of 1 K have been reported for micron sized particles in the presence of impurities [53]. Another recent study highlights the major impact of impurities on the rapid displacement (0.5 cm) over small time scales (120 s) of $1 \mu\text{m}$ silicon particles trapped in ice [54]. The objects investigated here are 1 order of magnitude (or

more) larger, which could explain why no regelation was observed. The use of cryo-confocal microscopy with the ability to image the solute segregation has a promising prospect for investigating such mechanisms. We believe the high space and temporal resolution can be used effectively to resolve the dynamics of individual colloidal particles to gain further insight into *regelation*.

4 Conclusions

In conclusion, we report that the oil droplets undergoing directional solidification feel the impact of solute at every stage, from being in the liquid phase to getting captured by the growing ice-water interface. The solute plays an important role in determining the droplet shape (deformed or not), droplet behaviour (engulfment or rejection), and eventually the droplet spatial distribution. To predict the solidified microstructure, an understanding of the several in-situ mechanisms at play is therefore indispensable. The use of rapid cryo-confocal microscopy facilitates an *in situ* investigation and quantification of solidification mechanisms with visualization of the local solute segregation. To represent the observations in real-life systems, we need to explore models incorporating interaction dynamics and object behaviour with solute effects. Current theories do not encompass all the factors required for explaining the long-range solute effects on the objects during solidification. We hope our experimental data can serve to improve the existing theoretical models. Finally, we suggest that the freezing of oil-in-water emulsions may serve as an analogue for studying the *in situ* interaction of foreign objects with an advancing solid-liquid interface in the presence of solute effects.

Acknowledgements

The research leading to these results has received funding from the ANRT and Saint-Gobain through a CIFRE fellowship (N° 2017/0774). We would like to

thank Alban Sauret and Virgile Thievenaz for discussing the deformation of droplets.

Author contributions

S.D. and C.M. designed and supervised the project, S.D, C.M. and S.T. designed the experiments, S.T. carried out the confocal microscopy, S.T., C.M. and S.D. analyzed the data. All authors discussed the results and implications and wrote the manuscript.

Corresponding Authors

Correspondence should be sent to Cécile Monteux (Cecile.Monteux@espci.fr) and Sylvain Deville (sylvain.deville@univ-lyon1.fr)

Conflict of interest

The authors declare no conflict of interest.

Availability of materials and data

The datasets generated during and/or analysed during the current study are available from the corresponding author on reasonable request.

References

- [1] Dash JG, Rempel AW, Wettlaufer JS. The physics of premelted ice and its geophysical consequences. *Reviews of Modern Physics*. 2006;78(3):695–741.
- [2] Rahman MS. *Handbook of food preservation*. CRC press; 2007.
- [3] Bronstein V, Itkin Y, Ishkov G. Rejection and capture of cells by ice crystals on freezing aqueous solutions. *Journal of Crystal Growth*. 1981;52:345–349.

- [4] Körber C. Phenomena at the advancing ice-liquid interface: solutes, particles and biological cells. *Quarterly reviews of biophysics*. 1988;21:229–298.
- [5] Zhang L. Nucleation, growth, transport, and entrapment of inclusions during steel casting. *Jom*. 2013;65(9):1138–1144.
- [6] Li H, Ghezal E, Nehari A, Alombert-Goget G, Brenier A, Lebbou K. Bubbles defects distribution in sapphire bulk crystals grown by Czochralski technique. *Optical Materials*. 2013;35(5):1071–1076.
- [7] Deville S. Freeze-casting of porous ceramics: a review of current achievements and issues. *Advanced Engineering Materials*. 2008;10(3):155–169.
- [8] Ghosh S, Coupland JN. Factors affecting the freeze–thaw stability of emulsions. *Food Hydrocolloids*. 2008;22(1):105–111.
- [9] Bunoiu O, Duffar T, Nicoara I. Gas bubbles in shaped sapphire. *Progress in crystal growth and characterization of materials*. 2010;56(3-4):123–145.
- [10] Shangguan D, Ahuja S, Stefanescu DM. An analytical model for the interaction between an insoluble particle and an advancing solid/liquid interface. *Metallurgical Transactions A*. 1992;23(2):669–680.
- [11] Asthana R, Tewari SN. The engulfment of foreign particles by a freezing interface. *Journal of Materials Science*. 1993;28(20):5414–5425.
- [12] Kim JK, Rohatgi PK. The effect of the diffusion of solute between the particle and the interface on the particle pushing phenomena. *Acta Materialia*. 1998;46(4):1115–1123.
- [13] Catalina AV, Sen S, Stefanescu DM, Kaukler WF. Interaction of porosity with a planar solid/liquid interface. *Metallurgical and Materials Transactions A*. 2004;35(5):1525–1538.
- [14] Tyagi S, Huynh H, Monteux C, Deville S. Objects interacting with solidification fronts: Thermal and solute effects. *Materialia*. 2020;12(April):100802.

- [15] Kao JCT, Golovin AA. Particle capture in binary solidification. *Journal of Fluid Mechanics*. 2009;625(September 2008):299.
- [16] Yang Y, Garvin J, Udaykumar H. Sharp interface numerical simulation of directional solidification of binary alloy in the presence of a ceramic particle. *International journal of heat and mass transfer*. 2008;51(1-2):155–168.
- [17] Wettlaufer J, Worster MG. Premelting dynamics. *Annu Rev Fluid Mech*. 2006;38:427–452.
- [18] Dedovets D, Monteux C, Deville S. Five-dimensional imaging of freezing emulsions with solute effects. *Science*. 2018;360(6386):303–306.
- [19] Fahy GM. The relevance of cryoprotectant "toxicity" to cryobiology. *Cryobiology*. 1986;23(1):1–13.
- [20] Sekhar JA, Trivedi R. Solidification microstructure evolution in the presence of inert particles. *Materials Science and Engineering A*. 1991;147(1):9–21.
- [21] Pötschke J, Rogge V. On the behaviour of foreign particles at an advancing solid-liquid interface. *Journal of Crystal Growth*. 1989;94(3):726–738.
- [22] Rempel AW, Worster MG. Interaction between a particle and an advancing solidification front. *Journal of Crystal Growth*. 1999;205(3):427–440.
- [23] Rempel AW, Worster MG. Particle trapping at an advancing solidification front with interfacial-curvature effects. *Journal of Crystal Growth*. 2001;223(3):420–432.
- [24] Park MS, Golovin AA, Davis SH. The encapsulation of particles and bubbles by an advancing solidification front. *Journal of Fluid Mechanics*. 2006;560:415–436.
- [25] Wei PS, Hsiao SY. Pore shape development from a bubble captured by a solidification front. *Int J Heat Mass Transf*. 2012 dec;55(25-26):8129–8138.

- [26] Ghezal EA, Li H, Nehari A, Alombert-Goget G, Brenier A, Lebbou K, et al. Effect of pulling rate on bubbles distribution in sapphire crystals grown by the micropulling down (μ -PD) technique. *Crystal Growth and Design*. 2012;12(8):4098–4103.
- [27] Jamgotchian H, Trivedi R, Billia B. Interface dynamics and coupled growth in directional solidification in presence of bubbles. *Journal of Crystal Growth*. 1993;134(3-4):181–195.
- [28] Sen S, Kaukler WF, Curreri P, Stefanescu DM. Dynamics of solid/liquid interface shape evolution near an insoluble particle - An X-ray transmission microscopy investigation. *Metallurgical and Materials Transactions A: Physical Metallurgy and Materials Science*. 1997;28(10):2129–2135.
- [29] Arbeloa FL, Ojeda PR, Arbeloa IL. Fluorescence self-quenching of the molecular forms of Rhodamine B in aqueous and ethanolic solutions. *Journal of luminescence*. 1989;44(1-2):105–112.
- [30] Dawson RMC, Elliott DC, Elliott WH, Jones KM. *Data for biochemical research*. vol. 3. Clarendon Press; 2002.
- [31] Harris EL, Angal S, Roe S. *Protein purification applications: a practical approach*. vol. 71. IRL press Oxford; 1990.
- [32] McNaught AD, Wilkinson A, et al. *Compendium of chemical terminology*. vol. 1669. Blackwell Science Oxford; 1997.
- [33] Schindelin J, Arganda-Carreras I, Frise E, Kaynig V, Longair M, Pietzsch T, et al. Fiji: an open-source platform for biological-image analysis. *Nature methods*. 2012;9(7):676.
- [34] van der Walt S, Schönberger JL, Nunez-Iglesias J, Boulogne F, Warner JD, Yager N, et al. scikit-image: image processing in Python. *PeerJ*. 2014 6;2:e453.

- [35] Dedovets D, Monteux C, Deville S. A temperature-controlled stage for laser scanning confocal microscopy and case studies in materials science. *Ultramicroscopy*. 2018;195(August):1–11.
- [36] Tiller WA, Jackson KA, Rutter JW, Chalmers B. The redistribution of solute atoms during the solidification of metals. *Acta Metallurgica*. 1953;1(4):428–437.
- [37] Anderson J, Lowell M, Prieve D. Motion of a particle generated by chemical gradients. Part 1. Non-electrolytes. *J Fluid Mech*. 1982;117(1):107–121.
- [38] Nery-Azevedo R, Banerjee A, Squires TM. Diffusiophoresis in ionic surfactant gradients. *Langmuir*. 2017;33(38):9694–9702.
- [39] Shimokusu TJ, Maybruck VG, Ault JT, Shin S. Colloid separation by CO₂-induced diffusiophoresis. *Langmuir*. 2019;36(25):7032–7038.
- [40] Shim S, Stone HA. CO₂-leakage-driven diffusiophoresis causes spontaneous accumulation of charged materials in channel flow. *Proceedings of the National Academy of Sciences*. 2020;117(42):25985–25990.
- [41] Lohse D, Zhang X. Physicochemical hydrodynamics of droplets out of equilibrium. *Nature Reviews Physics*. 2020;2(8):426–443.
- [42] Maass CC, Krüger C, Herminghaus S, Bahr C. Swimming droplets. *Annual Review of Condensed Matter Physics*. 2016;7:171–193.
- [43] Morozov M, Michelin S. Nonlinear dynamics of a chemically-active drop: From steady to chaotic self-propulsion. *The Journal of chemical physics*. 2019;150(4):044110.
- [44] Desai N, Michelin S. Instability and self-propulsion of active droplets along a wall. *Physical Review Fluids*. 2021;6(11):114103.
- [45] Shin S, Um E, Sabass B, Ault JT, Rahimi M, Warren PB, et al. Size-dependent control of colloid transport via solute gradients in dead-

- end channels. Proceedings of the National Academy of Sciences. 2016;113(2):257–261.
- [46] Wei PS, Huang CC, Wang ZP, Chen KY, Lin CH. Growths of bubble/pore sizes in solid during solidification—an in situ measurement and analysis. *J Cryst Growth*. 2004;270(3-4):662–673.
- [47] Maeno N. Air bubble formation in ice crystals. *Phys Snow Ice Proc*. 1967;1(1):207–2181.
- [48] Wei PS, Ho CY. An Analytical Self-Consistent Determination of a Bubble with a Deformed Cap Trapped in Solid during Solidification. *Metall Mater Trans B*. 2002;33(February):91–100.
- [49] Chernov A, Temkin D, Mel’Nikova A. The influence of the thermal conductivity of a macroparticle on its capture by a crystal growing from a melt. *Sov Phys Crystallogr*. 1977;22(6):656–658.
- [50] Sasikumar R, Ramamohan TR. Distortion of the temperature and solute concentration fields due to the presence of particles at the solidification front-effects on particle pushing. *Acta Metallurgica Et Materialia*. 1991;39(4):517–522.
- [51] Wettlaufer J. Impurity Effects in the Premelting of Ice. *Physical Review Letters*. 1999;82(12):2516–2519.
- [52] Rempel AW, Wettlaufer JS, Worster MG. Interfacial Premelting and the Thermomolecular Force: Thermodynamic Buoyancy. *Physical Review Letters*. 2001;87(8):088501.
- [53] Schollick J. Real space study of pattern formation in freezing colloidal suspensions. University of Oxford; 2012.
- [54] Marath NK, Wettlaufer JS. Impurity effects in thermal regelation. *Soft Matter*. 2020;16(25):5886–5891.